Evaporation of bi-component droplets in a heated, highly turbulent flow

Florian Moreau, Rudy Bazile

DOI 10.1007/s00348-012-1292-6

Evaporation of bi-component droplets in a heated, highly turbulent flow

F. Moreau · R. Bazile

Abstract This work aims to understand the phenomena that occur in a combustion chamber where multi-component fuel droplets are injected. Many evaporation models exist but the influence of turbulence on spray vaporization is not yet well understood. This study gives a useful database to improve these models. The objective of the work is to measure the dispersion and the evaporation of bi-component (octane/3-pentanone) droplets and the resulting vapor mixing in a well-known, heated, highly turbulent channel flow. The carrier flow shows high turbulence levels, flat profiles for the mean velocity and the velocity fluctuations. The injected droplets have a large variety of behaviors due to the large polydispersion and to the turbulence. The evolution of 3-pentanone liquid concentration, mass flux, and droplet clusters are described. Mean concentration, fluctuations of concentration, and mixing of the vapor phase are characterized.

1 Introduction

To reduce pollutant emissions and improve the performance of aeronautical combustion chambers, a better understanding of injection, atomization, evaporation, and mixing phenomena is required. A point of particular interest for combustion chamber designers is the question of ignition at high altitude where multi-component fuels are involved. In this study, we focus on the evaporation of bi-component droplets and the mixing of one of the component processes.

One of the first droplet evaporation models, proposed by Spalding (1951), describes a single-component, isolated droplet in a quiescent environment. Many authors have offered contributions to improve the description level of this model. For example, Hubbard et al. (1975) accounted for variable properties of the surrounding vapor. Also, Abramzon and Sirignano (1989) studied convection-driven effects and introduced modified Nusselt and Sherwood numbers. Then, Chiang and Sirignano (1993) took the wakes of the neighboring droplets into account. As for turbulence/droplet interaction, it seems to have contradictory effects. On the one hand, Birouk et al. (1996) showed that turbulence increases the isolated droplet evaporation rate. On the other hand, the formation of droplet clusters, because of turbulence, may locally increase the amount of vapor up to saturation and hinder or even stop the vapor production (Sornek et al. 2000). To provide keys for understanding what is occurring in an evaporating spray, experimental data are needed. The case of high turbulence levels, close to those encountered in a real combustion chamber, is studied here.

Finally, composition aspects have been addressed in a variety of ways, such as the discrete component model (Sirignano 1999), quite accurate but cumbersome, the Gamma Continuous Thermodynamic Model (Harstad et al. 2003), needing less computing time but lacking accuracy in the case of condensation, and the quadrature method of moments (McGraw 1997; Marchisio and Fox 2005), which is basically a combination of the other two methods. There is also a need for experimental data in the case of multi-component droplets, in order to improve these models.

The focus of this study is on the interaction of a spray with a highly turbulent, heated channel flow. In a previous

F. Moreau · R. Bazile (✉)
Université de Toulouse, INPT, UPS, IMFT (Institut de Mécanique des Fluides de Toulouse), Allée Camille Soula, 31400 Toulouse, France
e-mail: bazile@imft.fr

F. Moreau · R. Bazile
CNRS, IMFT, 31400 Toulouse, France

work (Cochet et al. 2009), the evaporation of mono-component droplets was investigated through the evolution of the vapor phase. In this paper, bi-component droplets (octane/3-pentanone, 85 and 15 %, respectively) are injected. First, the carrier flow properties are measured, and then, droplet dispersion and 3-pentanone concentration in the vapor and the liquid phase are characterized.

2 Experimental setup and laser techniques

2.1 Experimental setup

The experimental setup (Fig. 1) consists of two parts. The first one is a tank into which the heated air is injected, turbulence is generated, and a mist of droplets is created. The second is a channel with optical accesses in which the evaporation is studied using laser techniques.

The air is heated and injected at the top of the tank and passes through a turbulence generator before entering the channel. The turbulence generator has been adapted from a previous setup by Videto and Santavicca (1991); Bédat and Cheng (1995); Karpetis and Gomez (2000). It consists of a circular plate perforated by 45 holes 3 mm diameter and a convergent. The air passes through the holes. It creates 45 jets impacting on the convergent, which generates vortices that become mixed and then enter the channel. This leads to both turbulence levels much higher than classical grid turbulence: up to 40 % in the established zone, and good isotropic properties.

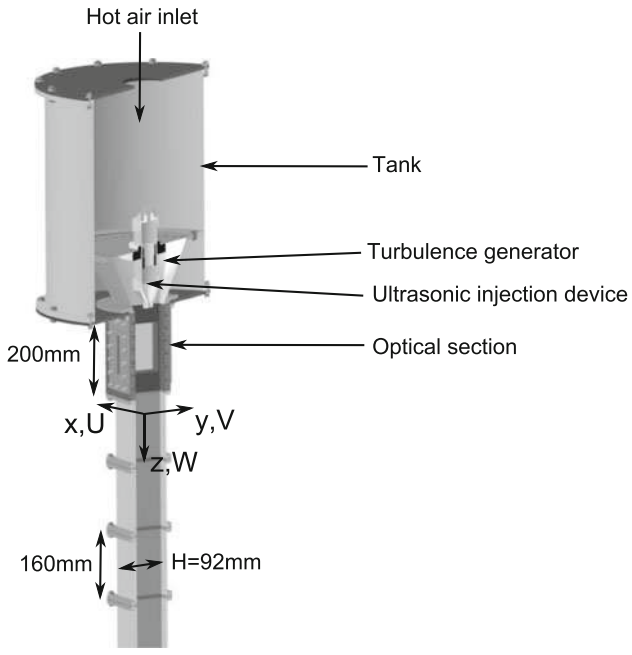

Fig. 1 Experimental setup

The channel is a 92 × 92 mm^2 square cross-section channel and is composed of four 160-mm-long segments and one optical segment. The optical segment is 200 mm long and equipped with two small quartz windows (100 × 10 mm^2; UV laser sheet is not absorbed by a quartz window) and two large Pyrex windows (110 × 82 mm^2) allowing optical measurements all along the channel. The z axis is the longitudinal axis, starting from the entrance of the channel. The y axis is the radial axis. Their origins are taken at the center of the square shaped cross-section. In the following sections, most results will be given versus z/H or y/H, where $H = 92$ mm is the width of the channel cross-section. The liquid injected is a mixture of 3-pentanone (15 %) and octane (85 %).

The velocity component along the z axis is the longitudinal velocity: W. The velocity component along y axis is the radial velocity: V. The mean in the sense of arithmetic average is represented by $\overline{W}$. The fluctuating part is $w' = W - \overline{W}$. The standard deviation is written: $w_{\mathrm{rms}} = \sqrt{\overline{w'^2}}$.

In order to create the droplet mist, an ultrasonic atomization device is placed at center of the channel, $x/H = y/H = 0$; the tip of the nozzle being located at $z/H = 0$. With this kind of atomizer, the liquid flow is disintegrated using ultrasounds, thus allowing small initial velocity for the droplets: $\sim$1 m/s whatever the size class is. The size range of droplets is large: from 0 to 250 µm. This leads to a large range of Stokes number, St, based on the Kolmogorov, τ_k, and the integral, T_e, time scale calculated in the established zone of the flow ($z/H = 4$) (see Sect. 3.2, Table 5). Therefore, many different behaviors are expected in the flow: from tracers to much more inertial droplets.

The carrier flow can be heated up to 423 K by an Osram heating resistance. A heating cord is put all around the tank to keep it warm and the whole test bench is insulated so as to prevent most of the heat losses. A thermal study has shown that the temperature decrease law along the longitudinal axis is 0.1 K/cm. The injection device is kept at atmospheric temperature with a water cooler surrounding it.

The experimental conditions are summarized in Table 1 and the thermodynamic properties of the components in Table 2.

2.2 Laser techniques

Three laser techniques are used in order to find the characteristics of the two-phase flow. Velocity fields of the continuous phase are determined with laser doppler anemometry (LDA). Velocities and diameters of the bi-component droplets (octane and 3-pentanone) are determined with phase doppler anemometry (PDA). The concentration of one of the two components, the 3-pentanone, in the liquid and vapor phases is determined with laser-induced fluorescence (LIF).

Table 1 Experimental conditions

Measurement of the continuous phase	Non-evaporating conditions
$T_{\text{incoming air}}$	293 ± 2 K
Bulk velocity W_0	2 ± 0.02 m/s
Measurement of the dispersed phase	**Evaporating conditions**
$T_{\text{incoming air}}$	423 ± 5 K
Bulk velocity W_0	2 ± 0.02 m/s
Air mass flux	14.3 ± 0.15 g/s
$T_{\text{incoming droplet}}$	293 ± 5 K
Liquid mass flux	0.322 ± 0.005 g/s
Volume fraction of 3-pentanone in the liquid mixture $V_{3\text{pentanone}}/(V_{3\text{pentanone}} + V_{\text{octane}})$	15 ± 0.1 %
Droplet mass fraction $\dot{m}_l/(\dot{m}_l + \dot{m}_g)$	2.2 %
Droplet volume fraction $\dot{V}_l/(\dot{V}_l + \dot{V}_g)$	2.5×10^{-5}

Table 2 Thermodynamic properties of octane and 3-pentanone

	Octane	3-pentanone
Molecular formula	C_8H_{18}	$C_5H_{10}O$
Boiling point (K)	399	374
Density (kg/m^3 at 293 K)	703	815
Dynamic viscosity (Pa s 10^{-6} at 293 K)	534	471
Specific heat (J/kgK at 293 K)	2,131	2,152
Thermal conductivity (Wm^{-1}K^{-1} at 293 K)	0.134	0.142

2.2.1 LDA measurements

Measurements are made using a two-component LDA system. The dimensions and characteristics of the LDA optical system are summarized in Table 3. A complete description of LDA and PDA measurement principles can be found in Albrecht et al. (2003).

In order to characterize the continuous phase, the inlet air is seeded with small oil droplets (1μm diameter) that are sensitive to turbulence at all scales. During these experiments, the air is not heated ($T_{\text{incoming air}} = 293$ K) to avoid evaporation of the oil droplets and the spray is not injected. Statistics are computed over 100,000 particles.

The so-called *velocity bias* is corrected through the use of transit time weighting (Hoesel and Rodi 1977; Buchhave et al. 1979).

2.2.2 PDA measurements

The measurement technique gives the velocity and diameter of each validated particle passing through the measurement volume. This enable us to obtain velocity statistics conditioned by the size of particles.

Table 3 Parameters of the LDA optical system

Transmitting and receiving optics	Laser 1/Laser 2
Wavelength of the laser	532/561 nm
Diameter of the laser beam	2.2/2.2 mm
Focal length of the front lens	159.8 mm
Beam separation	39.40/39.41 ± 0.02 mm
Diameter of the measuring volume	49/52 μm
Length of the measuring volume	402/424 μm
Fringe number	22
Fringe spacing	2.17/2.29 μm
Half angle	7.03°
Shift frequency	40 MHz

Table 4 Parameters of the PDA optical system

Transmitting optics	
Wavelength of the laser	532 nm
Diameter of the laser beam	2.2 mm
Focal length of the front lens	500 mm
Beam separation	39.40 ± 0.02 mm
Diameter of the measuring volume	154 μm
Length of the measuring volume	3.90 mm
Fringe number	22
Fringe spacing	6.76 μm
Half angle	2.26°
Shift frequency	40 MHz
Receiving optics	
Focal length of collimating lens	600 mm
Off-axis angle	27.5°
Maximum measurable diameter	370 μm
Width of spatial filter	193.5 μm

Measurements are made using a one-component PDA system. Dimensions and characteristics of the PDA optical systems are summarized in Table 4. During these experiments, the air is heated ($T_{\text{incoming air}} = 423$ K) and the injected spray is not heated ($T_{\text{incoming droplets}} = 293$ K). Statistics are computed over 50,000 droplets. The PDA system is optimized, in terms of laser beam power, photomultiplier voltage, signal gain as parameters, for the particle size range studied here using the suggestions of Kapulla and Najera (2006) and Albrecht et al. (2003).

During the experiment, the tank and the air are heated. This induces a gradient of refractive index in the optical access and in the flow inside the channel. This gradient generates a deviation of the laser beams. From the classical LDA and PDA formula (Albrecht et al. 2003), the logarithmic derivation shows very small sensitivity (0.1 %) of

the measured velocity and diameter to the refractive index gradient.

The droplets are also heated. In consequence, the proportion of 3-pentanone, which is the more volatile component, decreases during the evaporation process. As the two components have two different refractive indices, there is a variation of the refractive index of the mixture. The range of variation of refractive index due to change in concentration has to be considered from a concentration of 15 % of 3-pentanone in the initial mixture to pure octane.

The temperature also has an influence on the refractive index of each component. Simulations of a monodispersed spray show that the saturation temperature of the droplets should not exceed 353 K. This was confirmed using global rainbow thermometry (Bodoc et al. 2009). The range of variation of refractive index due to the change of temperature has to be considered for a temperature from 293 to 353 K.

Measurements performed by Bodoc (2011) are linearly interpolated over the range 293–326 K and extrapolated over the range 326–353 K (Fig. 2). The variation of refractive index due to both temperature and concentration remains in the range $n = [1.366–1.394]$. These changes of refractive index have a direct influence on the measurement of the diameter. The relation (Albrecht et al. 2003) used to calculate the diameter of a particle, d_p, from the measured phase difference between photodetectors 1 and 2, $\Delta\Phi_{12}$, for first-order refraction, is:

$$\begin{aligned}\Delta\Phi_{12} &= \beta_{12} d_p \\ &= 2\frac{2\pi}{\lambda} d_p \left(\sqrt{1 + m^2 - m\sqrt{2}\sqrt{1 + \cos\psi_r \cos\phi_r \cos\theta/2 + \sin\psi_r \sin\theta/2}} \right. \\ &\left. - \sqrt{1 + m^2 - m\sqrt{2}\sqrt{1 + \cos\psi_r \cos\phi_r \cos\theta/2 - \sin\psi_r \sin\theta/2}} \right)\end{aligned} \tag{1}$$

where ψ_r is the detector elevation angle of the system, θ the intersection angle of the laser beams, ϕ_r the scattering angle, β_{12} the diameter conversion factor, m the relative refractive index ($m = n/n_m$ where n is the refractive index of the particle and n_m the refractive index of the air). The variation of diameter conversion factor for different refractive indexes and for several scattering angles is plotted in Fig. 3. For the scattering angle used in the experiment, 27.5°, and the range of refractive index, a variation of 5 % is calculated. In conclusion, compared to the case of mono-component droplets at constant temperature, the additional uncertainty due to the variations in liquid composition and temperature never exceeds 5 %.

2.2.3 LIF measurements

The concentration of 3-pentanone in the liquid and vapor phase is determined using LIF. The LIF technique is based on the physical phenomenon of fluorescence. When fluorescent molecules are excited by a laser beam at a well-chosen wavelength, λ, they emit a fluorescence signal, S, over a range of wavelength longer than the excitation wavelength, thus allowing the fluorescent emission to be distinguished from Mie scattering. Since the number of photons emitted is proportional to the number of molecules excited, N, it is possible to obtain a direct measurement of the molecular concentration. However, the quenching, linked to the pressure and temperature conditions (P and T), has an influence on the fluorescence signal. There is no pressure variation during the experiment. The influence of the temperature is discussed below.

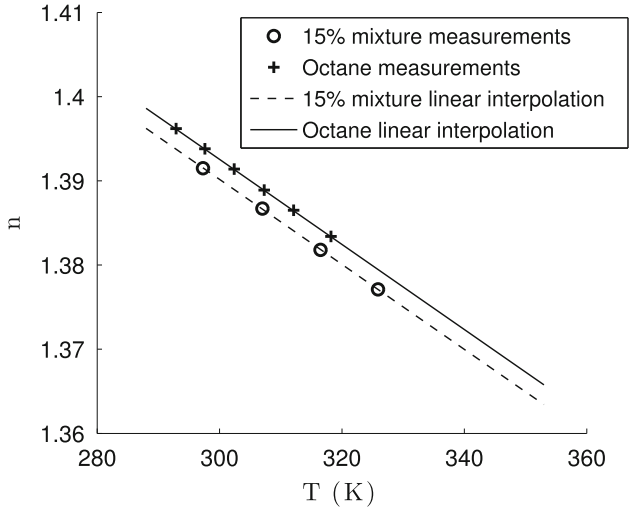

Fig. 2 Variation of the refractive index of the droplets versus temperature for the 3-pentanone/octane mixture and for pure octane. Measurements are linearly interpolated

The emitted fluorescence signal can be written as below (Eq. 2):

$$S(x, \lambda, T, P, N) = I_0 N(x) \sigma(\lambda, T) \phi_q(\lambda, T, P, N) e^{-\sigma \int N(x) \mathrm{d}x} \tag{2}$$

where σ is the molecular absorption cross-section of the molecule, and ϕ_q is the fluorescence quantum yield.

The laser used for LIF experiments is a pulsed Nd:YAG laser: $\lambda = 266$ nm, $e = 30$ mJ, $f = 10$ Hz. A vertical laser sheet is generated with a thickness of about 400 µm. The fluorescence signal is collected with a 16 bit, 1,024 × 1,024 pixel intensified camera (PI-MAX Princeton) and a 58-mm objective lens. A 300–500 nm band-pass filter, BG-25, is used to remove Mie scattering from the droplets. In these experimental conditions, no fluorescence signal is emitted by octane or air.

The fluorescent molecule used in this study is 3-pentanone. Its photo-physical properties have been widely studied (Koch and Hanson, 2003; Modica et al. 2007) in

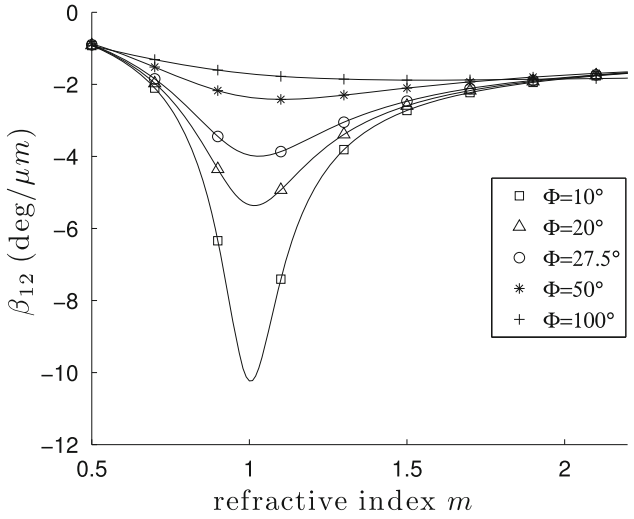

Fig. 3 Variation of the conversion phase factor, β_{12}, versus refractive index for different off-axis angles, ϕ: 10°, 20°, 27.5° (used in the experiment), 50° and 100°

vapor phase. The UV absorption spectrum of 3-pentanone extends from 230 to 340 nm with a peak at 285 ± 5 nm for a range of temperatures between 298 and 423 K. The 3-pentanone fluorescence signal is emitted between 350 and 550 nm with a maximum at 420 nm. As these two spectra do not overlap, there is no fluorescence trapping.

According to Koch and Hanson (2003), between 298 and 423 K, the influence of temperature on the fluorescence signal per molecule, under nitrogen, is small: less than 5 %. According to Orain et al. (2008), the quenching of the fluorescent signal due to the presence of oxygen over this range of temperatures is negligible. Then, the influence of temperature on the fluorescence signal, in atmospheric conditions, is less than 5 %. In this experiment, the fluorescence signal can be simplified: $S(x, \lambda, T, P, N) = S(x, N)$

The only remaining bias is the dependency of the signal on the radial position, x, from the entrance of the laser beam into the channel: $x = 0$, due to absorption of the incident laser beam. This absorption of the laser is corrected along each radial line of the x axis. The signal of fluorescence can be written in discrete form:

$$S(x,N) = I_0 \Phi \sigma N(x) e^{-\sigma \sum_{x'=0}^{x'=x} N(x')\Delta x'} \quad (3)$$

The ratio R is defined at the entrance of the laser in the channel by $R = I_0 \Phi \sigma = S_f(0)/N(0)$.

Then, Eq. 4 is used to correct absorption pixel by pixel up to the end of the radial line.

$$N(x) = \frac{S_f(x)}{R} e^{\sigma \sum_{x'=0}^{x'=x} N(x')\Delta x'} \quad (4)$$

In order to validate this procedure, the algorithm is used to correct the absorption in the channel filled with saturated vapor of 3-pentanone. The deviation from the expected signal along the radial line is less than 1 %. This correction is then applied to each instantaneous LIF image.

The uncertainty during the calibration of the signal is around 5 %. The fluctuation of the laser energy from one shot to another is 5 %. Thus, for the vapor phase, the overall uncertainty for the mean concentration measurement is 10 % and for the fluctuation of concentration it reaches 15 %.

Concerning the fluorescence of the liquid phase, no data have been found in the literature. An experiment is performed, using a quartz cell, to find the relation between the fluorescent signal and the 3-pentanone concentration in the liquid phase. Several concentrations of 3-pentanone are used in the range [3–15 %]. This is done for several temperatures in the range [305–333 K] (Fig. 4). As previously explained, simulations on a monodispersed spray and experiments (Bodoc et al. 2009) have shown that the saturation temperature of the droplets should not exceed 353 K. Therefore, the range of temperature studied remains valid for the spray conditions. The effect of temperature on the fluorescent signal is around 5 %. Moreover, the signal is found to be proportional to the concentration with a deviation from linearity that never exceeds 5 %. The only parameter that is changed during the calibration, compared with the spray conditions, is the aperture of the optical system. Then, another experiment is performed to check the linearity of the system. A maximal deviation of 5 % from linearity is measured. No effect of absorption is measured when analyzing the droplets into the spray. This is due to the small volume fraction of the dispersed phase, $\sim 10^{-5}$. Thus, no absorption correction is needed for the dispersed phase.

In conclusion, the overall uncertainty for the LIF measurements of 3-pentanone in the liquid phase is 15 %.

3 Dispersion of the droplets in a highly turbulent flow

3.1 Continuous phase

The axial variation of the normalized mean longitudinal velocity at the center of the channel (Fig. 5) shows three areas: a first zone with a strong decrease in the velocity from the entrance to $z/H = 2$; a second zone with an increase in the velocity up to $z/H = 4$ and, finally, a quasi established zone in which the longitudinal velocity remains constant.

To go further into the analysis of the mean flow behavior, radial profiles of the mean longitudinal velocity

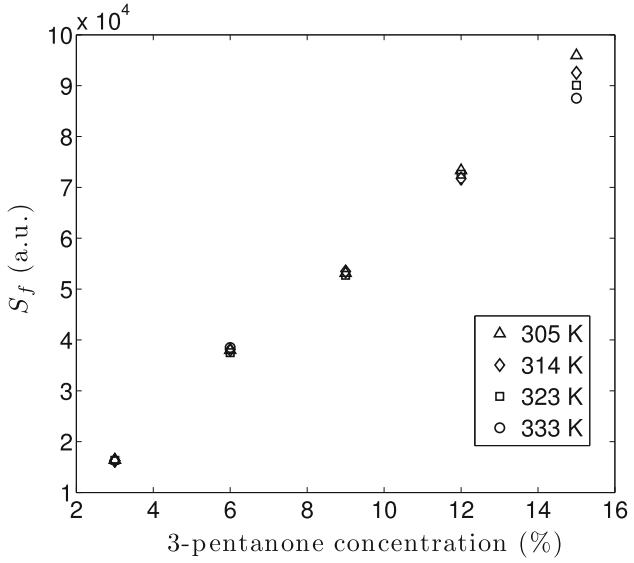

Fig. 4 Fluorescence signal versus 3-pentanone concentration in octane, with liquid temperature as parameter: 305, 314, 323, and 333 K

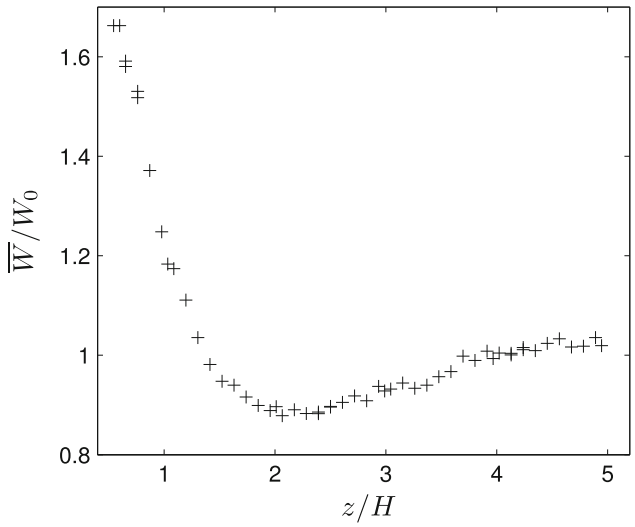

Fig. 5 Axial variation at $x = y = 0$ of the normalized mean longitudinal velocity $\overline{W}/W_0$

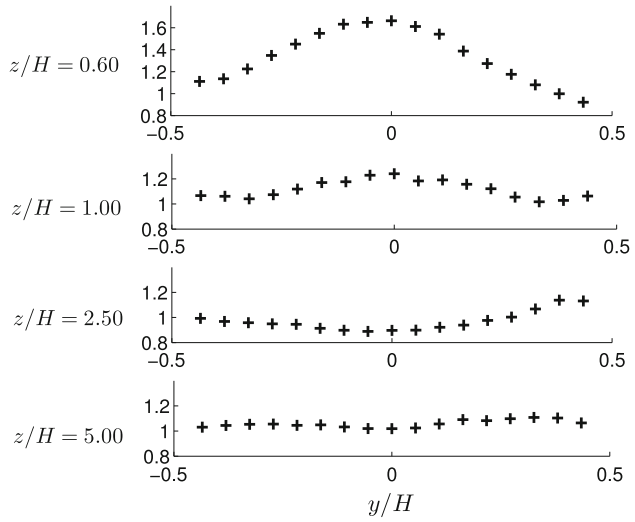

Fig. 6 Radial variation of the normalized mean longitudinal velocity $\overline{W}/W_0$ at several axial locations

are plotted (Fig. 6). After the entrance of the channel, $z/H = 0.60$, the higher velocity at the center of the profile is balanced by low velocity close to the wall. This effect decreases downstream with an inversion of the profile at $z/H = 2.50$. Beyond, the profiles can be considered as flat.

The fluctuations of the longitudinal and radial velocities are of the same order of magnitude (Fig. 7). Except at the first stage after the entrance of the channel, $z/H = 0.60$, the profiles are flat and get closer downstream.

The isotropy properties are quantified (Fig. 8) on the centerline through the isotropy coefficient: $v_{\mathrm{rms}}/w_{\mathrm{rms}}$. In the ideal case of isotropic turbulence: $v_{\mathrm{rms}}/w_{\mathrm{rms}} = 1$. Beyond $z/H = 1.5$, the coefficient of isotropy measured never exceeds a difference of 10 % from this ideal value. In the case of isotropic turbulence, there is no correlation between the radial and the longitudinal fluctuations and the Reynolds stresses: $\overline{w'v'}/(w_{\mathrm{rms}}v_{\mathrm{rms}}) = 0$. Beyond $z/H = 1.5$, the Reynolds stresses measured (Fig. 8) never exceed a difference of 10 % from this ideal value. The intensity of the turbulence is usually defined as $I = \frac{\sqrt{\overline{w'^2}+\overline{v'^2}+\overline{u'^2}}}{\sqrt{\overline{W}^2+\overline{V}^2+\overline{U}^2}}$. Using a hypothesis of axisymmetry on the centerline, the intensity of the turbulence is defined here as $I = \frac{\sqrt{\overline{w'^2}+2\overline{v'^2}}}{\sqrt{\overline{W}^2+2\overline{V}^2}}$. In grid turbulence, the intensity levels rarely exceed 10 %. The intensity measured in this experiment (Fig. 8) is 100 % at the entrance of the channel ($z/H = 0.6$) and 40 % in the established zone ($z/H = 4.0$).

According to a previous work (Cochet 2007), the integral length scale (at $z/H = 4.0$) is 25mm and the Kolmogorov length scale is 160 µm. The Reynolds number based on the width of the channel is $Re_H = 12{,}000$, and the turbulent Reynolds number based on the integral length scale is 650.

3.2 Dispersed phase

During a PDA measurement, when a droplet crosses the measurement volume, its velocity and diameter become available. This provides velocity statistics conditioned by the size classes. In order to study the droplet behavior conditioned by the size class, the diameter distribution is divided into four parts (Fig. 9). The corresponding Stokes numbers based on the Kolmogorov, τ_k, and on the integral,

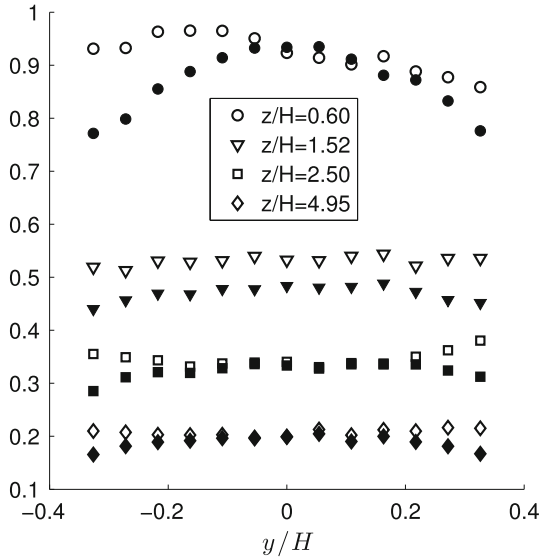

Fig. 7 Radial variation of w_{rms}/W_0 (*empty symbol*) and v_{rms}/W_0 (*filled symbol*) at several axial position: $z/H = 0.60$, $z/H = 1.5$, $z/H = 2.5$, $z/H = 5$

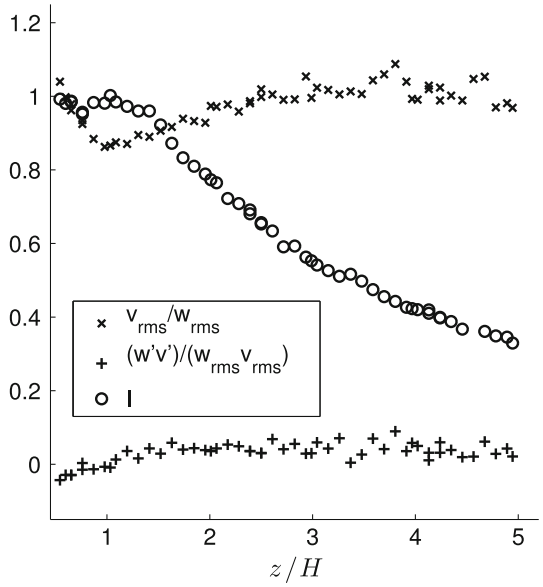

Fig. 8 Axial variation at $x = y = 0$ of the the Reynolds stresses, the isotropy coefficient, v_{rms}/w_{rms}, and the intensity of the turbulence, I

T_e, time scales are calculated in the established zone of the flow ($z/H = 4$) and are reported in Table 5.

The variation of the mean longitudinal velocity of the droplets is presented in Fig. 10. Except at the first stage after the injection zone ($<z/H = 0.6$), the droplets linked to the smallest size class follow the air flow. However, the droplets linked to the biggest size class increase their velocities up to the final velocity. Intermediate behaviors are found for the droplets of intermediate size classes.

The fluctuations of the longitudinal velocity (Fig. 11) lead to the same conclusions. The droplets linked to the smallest size class follow the fluctuations of the continuous phase quite well. On the other hand, the droplets from the biggest size class have much greater inertia and their fluctuations show only a small change. As previously, the droplets of intermediate size classes have two intermediate behaviors.

These behaviors can be understood through the Stokes numbers of the droplets (Table 5). The smallest droplets follow all the length scales of the flow whereas the biggest have much greater inertia.

4 Evolution of the 3-pentanone in the liquid and vapor phases

Two of the main issues in two-phase flow combustion are the evolution of the liquid and vapor fluxes due to the evaporation process and the mixing of the vapor phase. During the combustion process, if the vapor concentration is locally inhomogeneous, this can lead to extinction of the flame or to the creation of undesirable polluting components or soot. To prevent these phenomena, the question of homogeneity of the vapor phase has to be investigated. As can be seen in Fig. 12, at the beginning of the channel (a), there are many evaporating droplets and the vapor is inhomogeneous. Going downstream (b), there are fewer

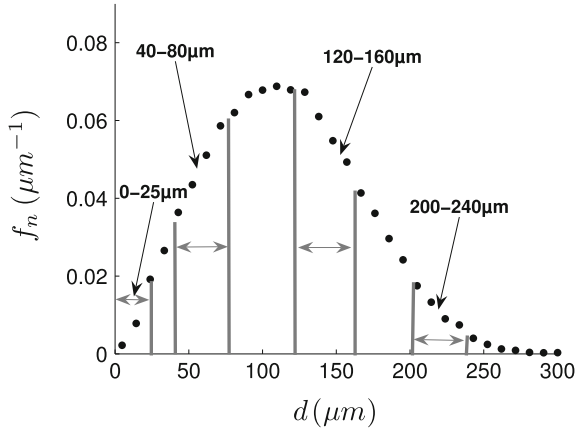

Fig. 9 Diameter PDF at $z/H = 0.55$ and size classes definition

Table 5 Stokes number based on integral time scale, St_{T_e}, and Kolmogorov time scale, St_{τ_k}, for several diameter ranges

Diameter range (µm)	0–25	40–80	120–160	200–240
St_{T_e}	7.5×10^{-3}	0.15	0.70	1.5
St_{τ_k}	2.2×10^{-1}	4.5	20	42

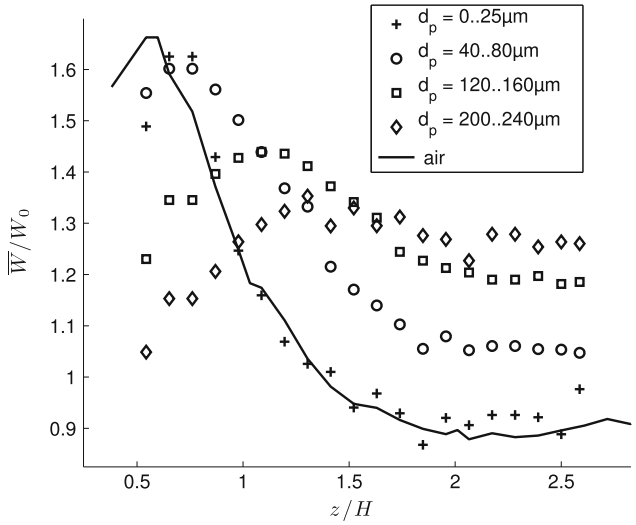

Fig. 10 Axial variation of normalized mean longitudinal velocity, at $x = y = 0$, for air (measured at 293 K) and droplets per size class: 0–25, 40–80, 120–160, 200–240 µm

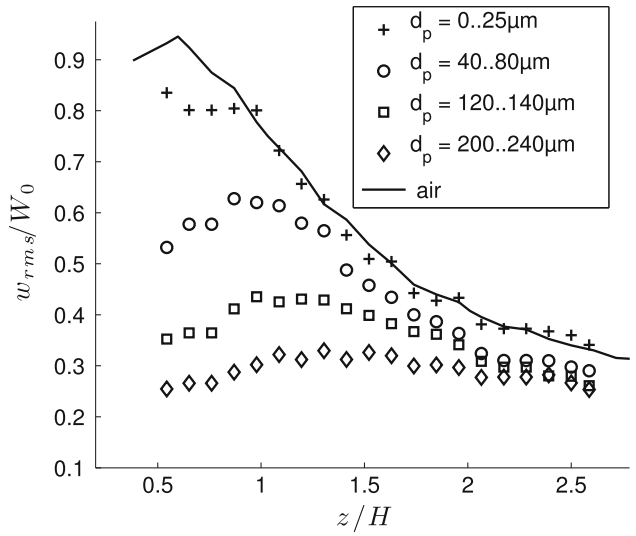

Fig. 11 Axial variation of normalized rms longitudinal velocity, at $x = y = 0$, for air (measured at 293 K) and droplets per size class: 0–25, 40–80, 120–160, 200–240 µm

and fewer droplets and the vapor becomes much more homogeneous. The first step is thus to extract the liquid and vapor phases before analysis.

4.1 Liquid: vapor phase discrimination

Some techniques exist to discriminate between the liquid and vapor phases on instantaneous LIF images.

For example, a threshold can be used. In some experimental cases, the gray scale level histogram shows two peaks: one concerning the liquid phase and the other concerning the vapor phase. However, in the case studied here,

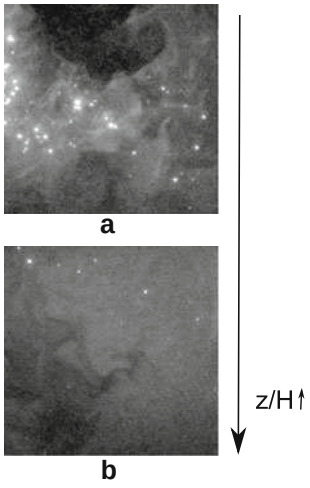

Fig. 12 Instantaneous images of fluorescence of 3-pentanone at z/H = 1.5 (**a**) and z/H = 5 (**b**)

there is only one large peak. This is due to the fact that the lowest liquid signal reaches the value of the highest vapor signal. This method of discrimination is thus not relevant in the present case. Another option is to choose a threshold based on the value of the signal emitted by saturated vapor of 3-pentanone. Values above this threshold correspond to the liquid phase. However, droplets with a small amount of 3-pentanone or droplets crossing the edge of the laser sheet (with a low energy) will give values below this threshold. Some liquid will be considered as vapor, leading to an error in measurement.

The technique used here is a discrimination method based on median filtering (using a 7 × 7 structuring element). The filtered image is subtracted from the input image. The result is an image containing the high spatial frequencies. After morphological treatments, threshold, dilation and erosion, a binary image, representing the shape of the droplets, is obtained. The input image is multiplied by the binary image (where 1 is the value of a pixel representing liquid). The product is an image with the liquid information only. The same procedure is applied, using the negative of the binary image, to obtain information on the vapor phase (Fig. 13). For more details see Moreau (2010).

The signal from the 3-pentanone in the liquid phase is much higher (approximately 100 times) than the signal in the vapor phase so that the two phases cannot be measured accurately with the same optical setting. Therefore, the LIF measurements are divided into two parts.

Before $z/H = 3$, the high liquid concentration requires a small aperture of the optical system, to avoid saturation of the camera. When this setting is used, the signal of the vapor phase is to close to the noise to be measured accurately.

Beyond $z/H = 3$, another setting is used to measure the fluorescent signal from the vapor phase, with a larger

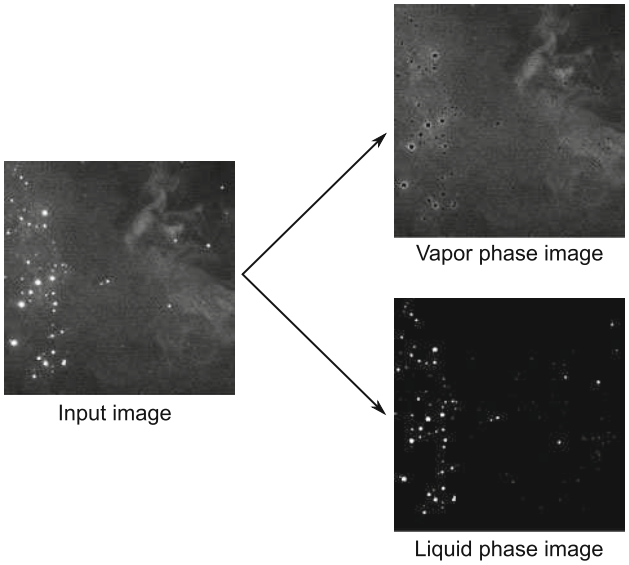

Fig. 13 Liquid–vapor phase discrimination

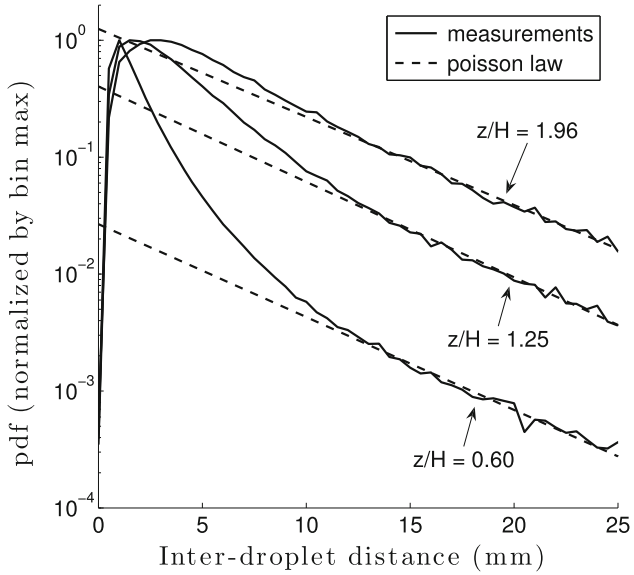

Fig. 14 Distribution of inter-droplet distances, measurements and corresponding Poisson law

aperture of the optical system. The signal of the liquid saturates the camera but is filtered by the post-treatment. Such saturation is dangerous for the camera in the first area but in the second area, beyond $z/H = 3$, the amount of liquid is small enough to prevent the deterioration of the camera. However, the amount of droplet is too small to obtain well-converged data on the liquid phase using the second setting. This is why no measurement of the vapor phase is available before $z/H = 3$ and no measurement of the liquid phase beyond $z/H = 3$.

4.2 Dispersion and evaporation of the 3-pentanone in the liquid phase

The algorithm previously described is used to determine the position of each droplet and the distance between droplets is measured.

The uniform and random distribution of tracers in a flow follows the Poisson law (Erdmann and Gellert 1976). The distance between two droplets and the corresponding Poisson law (with the same density of droplet) is represented in Fig. 14. In order to compare the PDFs (Probability density functions), they are normalized by the maximal bin of the vertical axis.

There are more short distances between droplets than predicted for a uniform, random distribution. This can be explained by the presence of clusters. This effect, and thus the amount of clusters, decreases downstream. These clusters may be due to a combination of both pulsation of the air flow in the wake of the injection device and to effect of the turbulence on the droplets.

The mean concentration of 3-pentanone in the liquid phase is presented in Fig. 15. At the entrance of the

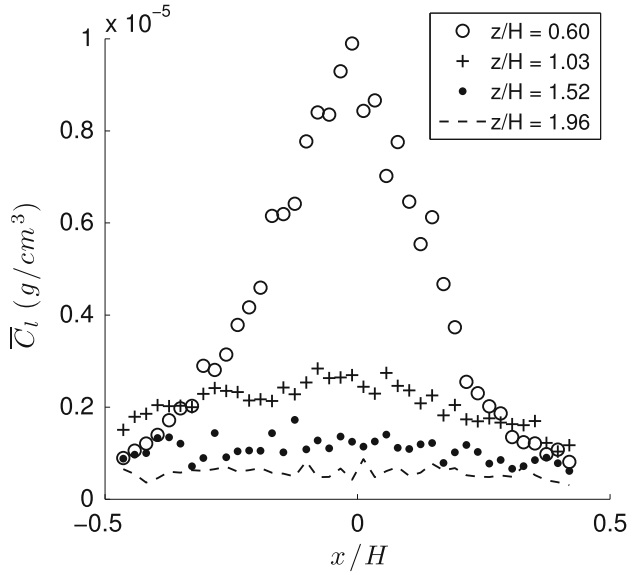

Fig. 15 Radial profiles of the mean concentration of 3-pentanone in the liquid phase at $z/H = 0.60$, 1.03, 1.52 and 1.96

channel ($z/H = 0.60$), most of the liquid is located on the centerline of the channel due to the central position of the injection. The peak enlarges and decreases downstream due to both dispersion and phase change.

Assuming axisymmetry and using the value of the mean volume velocity obtained in the liquid phase (Eq. 5), the mean concentration of 3-pentanone in the liquid phase is integrated over the cross-section of the channel. The associated mass flow rate is then calculated (Eq. 6). Its interpolation shows an exponential decrease (Fig. 16; Eq. 7):

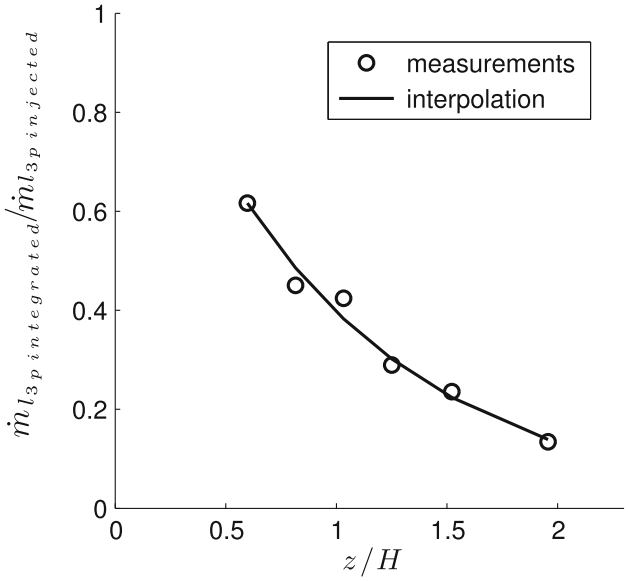

Fig. 16 Axial evolution of normalized mass flow rate of 3-pentanone in the liquid phase, measurements: *circle*, interpolation: *solid line*, where the interpolation law is $\dot{m}_{l_{3\text{p integrated}}}/\dot{m}_{l_{3\text{p injecte}}} \propto e^{-1.1\frac{z}{H}}$

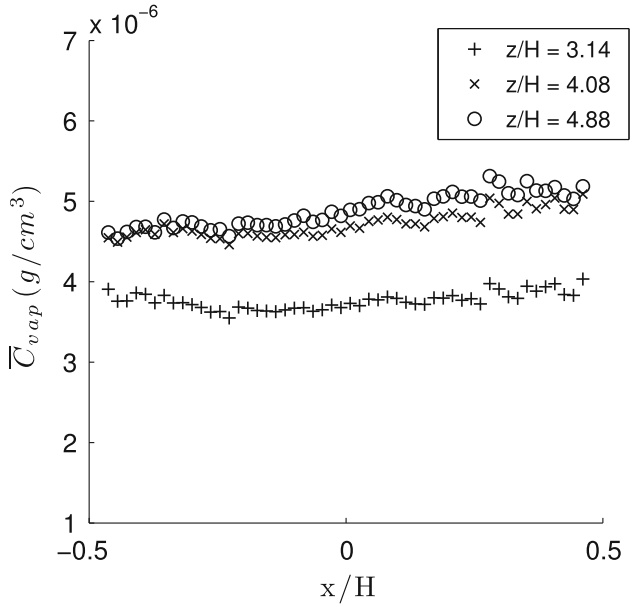

Fig. 17 Radial profiles of the mean concentration of 3-pentanone in the vapor phase at $z/H = 3.14$, 4.08 and 4.88

$$\overline{W}_{\text{vol}} = \frac{\sum_{j=1}^{n_{\text{echant}}} W_j d_j^3}{\sum_{j=1}^{n_{\text{echant}}} d_j^3} \tag{5}$$

$$\begin{aligned} \dot{m}_{l_{3\text{p integr}}} &= \int_0^{\frac{H}{2}} \int_0^{2\pi} \overline{C}_l(r,\theta)\overline{W}_{vol}(r,\theta) r \mathrm{d}r\mathrm{d}\theta \\ &= 2\pi \int_0^{\frac{H}{2}} \overline{C}_l(r)\overline{W}_{vol}(r) r \mathrm{d}r \end{aligned} \tag{6}$$

$$\dot{m}_{l_{3\text{p integrated}}}/\dot{m}_{l_{3\text{p injecte}}} \propto e^{-1.1\frac{z}{H}} \tag{7}$$

4.3 Evolution of the concentration of 3-pentanone in the vapor phase

The radial profiles of the mean concentration of 3-pentanone in the vapor phase (Fig. 17) are flat from $z/H = 3.14$. The small asymmetry can be explained by the absorption of the laser signal by the medium, which is not perfectly corrected.

The same integration is used to calculate of the mass flow rate of the vapor phase (Fig. 18), except that the bulk velocity is used as the mean velocity. The value 1 of the normalized mass flow rate corresponds to a value where the liquid phase is completely vaporized. The mass flow rate measured reaches the value of 0.93. This is because not all the droplets are vaporized at the end of the channel (as can be seen in Fig. 12b).

The radial profiles of rms concentration of 3-pentanone in the vapor phase are flat from $z/H = 3.14$ (Fig. 19). The longitudinal evolution, on the centerline, of rms concentration of 3-pentanone in the vapor phase (Fig. 20) shows a decrease. This decrease follows a power law (Eq. 8). It

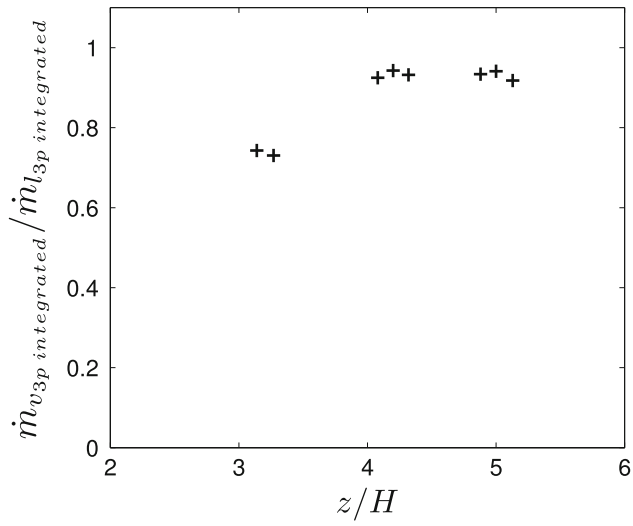

Fig. 18 Axial evolution of normalized mass flow rate of 3-pentanone in the vapor phase

corresponds to a temporal homogenization of the 3-pentanone concentration.

$$c_{\text{vap rms}}/\overline{C}_{\text{vap}} \propto z/H^{(-0.60)} \tag{8}$$

An experiment is then carried out to see the influence of the creation of vapor by the droplets. The injector is removed. The vapor is injected at the entrance of the channel through the cooling device. The vapor and the air velocity are the same, and the total mass flow rate (air and vapor) remains the same as in the two-phase-flow

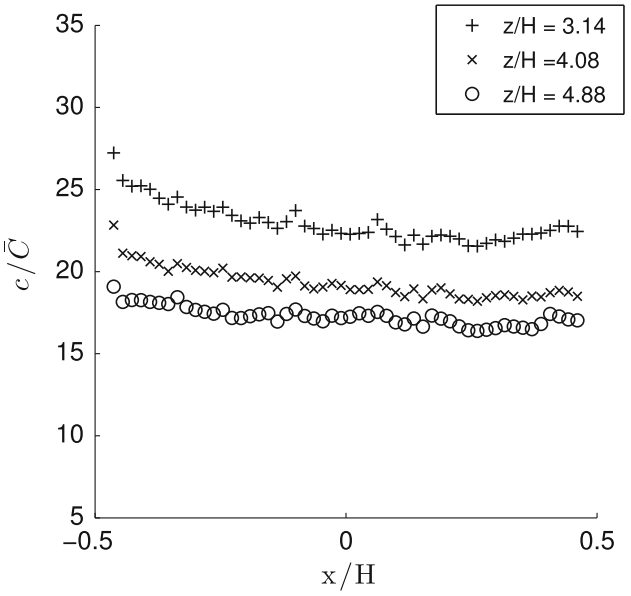

Fig. 19 Radial profiles of the rms concentration of 3-pentanone in the vapor phase at $z/H = 3.14$, 4.08 and 4.88

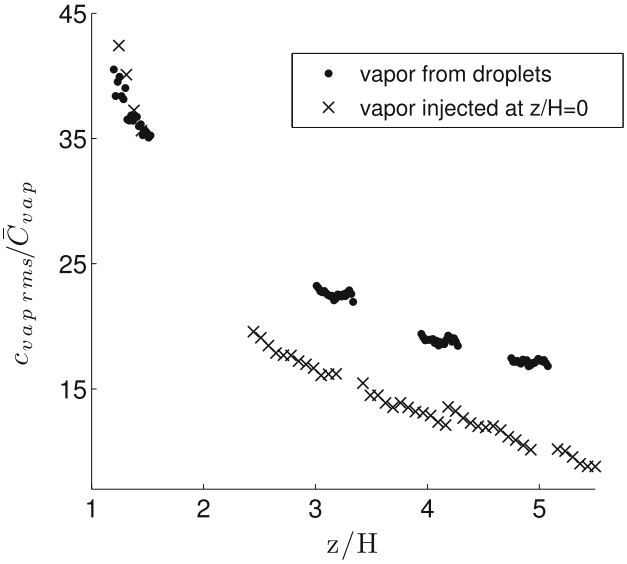

Fig. 20 Longitudinal evolution of the rms concentration of 3-pentanone in the vapor phase. Comparison between the vapor from droplets and vapor injected at the entrance of the channel

experiment. The mixing is more efficient in the case of vapor injected at the entrance of the channel (Fig. 20). A possible explanation is that droplets are sources of vapor and so sources of inhomogeneity.

To ensure a good combustion environment, a good level of spatial homogeneity has to be achieved. Fig. 12 shows instantaneous images of the 3-pentanone concentration in the vapor phase at the entrance (a) and at the end (b) of the channel. At the entrance, pockets of air can be seen (in black), whereas at the end of the channel, the concentration of 3-pentanone is much more homogeneous from the spatial point of view. In order to quantify the spatial homogeneity, an operator of radial variance, $\overline{\sigma}_c$, is defined (see Eq. 10). $c_{i,n}$ is the concentration of the nth image, for the radial pixel i on the radial middle-line of the image and $\langle\rangle$ is the radial mean operator.

$$\sigma_{c_n} = \frac{1}{\langle c_n \rangle} \sqrt{\frac{1}{I_{\text{pixel}}} \sum_{i=1}^{I_{\text{pixel}}} (c_{i,n} - \langle c_n \rangle)^2} \tag{9}$$

$$\overline{\sigma}_c = \frac{1}{N_{\text{image}}} \sum_{n=1}^{N_{\text{image}}} \sigma_{c_n} \tag{10}$$

$\overline{\sigma}_c$ is equal to zero for radially homogeneous concentration and increases with the spatial heterogeneities.

The axial evolution of the spatial homogeneity operator is shown in Fig. 21. As expected, there is a homogenization from the spatial point of view as well. The rms concentrations of the 3-pentanone in the vapor phase are integrated radially and compared with the spatial homogeneity operator. It is found that the decrease in temporal and spatial concentrations is of the same order of magnitude.

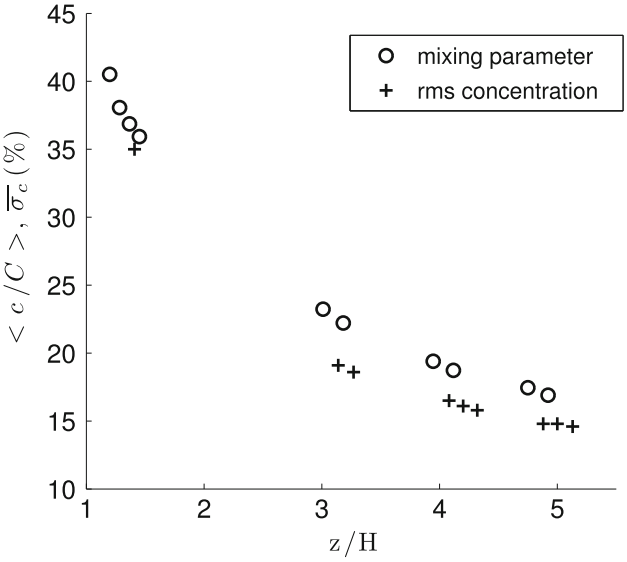

Fig. 21 Axial evolution of the mixing parameter, $\overline{\sigma}_c$, and the normalized rms concentration of 3-pentanone in the vapor phase, $\langle c_{\text{vap rms}}/\overline{C}_{\text{vap}} \rangle$

5 Conclusions

An experimental setup generating high levels of turbulence is used to study the evaporation of bi-component (octane/3-pentanone) droplets in a heated channel flow.

The continuous phase shows flat profiles for mean velocities after a distance of $z/H = 2.5$ and for fluctuations from $z/H = 1.5$. From $z/H = 1.5$, the flow presents isotropic properties: on the centerline, the fluctuations of the

longitudinal and radial component of the velocity are of the same order and are uncorrelated. The turbulence levels generated are high, from 100 % at the entrance of the channel to 40 % in the established zone.

Due to the large range of Stokes numbers, the droplets exhibit wide variety of behaviors from tracers to much more inertial behavior.

Through appropriate filtering and calibration, the 3-pentanone concentration in the liquid and vapor phase is discriminated and measured by means of the LIF technique. The evolution of the evaporating 3-pentanone in the liquid phase is analyzed in terms of concentration. The corresponding fluxes are calculated through a coupling with PDA measurements, and an exponential decrease in the liquid mass flux is found. Clusters are notable at the entrance of the channel, but their amount decrease downstream due to the dispersion in the flow.

The evolution of the 3-pentanone in the vapor phase shows flat radial profiles for the mean concentration from $z/H = 3.14$. 93 % of the 3-pentanone injected is measured at the end of the channel ($z/H = 5$). The radial profiles for the rms or temporal fluctuation are also flat. The decrease in the rms fluctuations, i.e., the temporal homogenization, on the centerline, follow a power law. The temporal fluctuations of the concentration coming from the droplets are compared with those of vapor injected at the entrance of the channel. The droplets, creating vapor as they go downstream, induce less efficient mixing. The spatial homogeneity is quantified through an operator (the radial variance of concentration) and compared with the temporal evolution. They are found to be of same order of magnitude.

Acknowledgments M. Marchal, G. Couteau, S. Cazin, E. Cid, and all the people of the mechanical workshop are gratefully thanked for their technical support. This project was funded by the PFA-ASTRA program, a collaboration between the CNRS and ONERA institutions.

References

Abramzon B, Sirignano W (1989) Droplet vaporization model for spray combustion calculations. Int J Heat Mass Transf 32(9): 1605–1618

Albrecht HE, Borys M, Damaschke N, Tropea C (2003) Laser doppler and phase doppler measurement techniques. Springer, New York

Bédat B, Cheng RK (1995) Experimental study of premixed flames in intense isotropic turbulence. Combust Flame 100(3):485–494

Birouk M, Chauveau C, Sarh B, Quilgars A, Gokalp I (1996) Turbulence effects on the vaporization of monocomponent single droplets. Combust Sci Technol 113(1):413–428

Bodoc V (2011) Multicomponent droplet vaporization. PhD thesis, ISAE

Bodoc V, Moreau F, Biscos V, Basile R, Lavergne G (2009) Experimental investigation of evaporating bi-component droplets in a turbulent channel flow. International annual conference on liquid atomization and spray systems, Vail, Colorado, USA

Buchhave P, George WK, Lumley J (1979) The measurement of turbulence with the laser-doppler anemometer. Annu Rev Fluid Mech 11:443–503

Chiang C, Sirignano W (1993) Axisymmetric calculation of three droplets interactions. Atomization Sprays 3:91–107

Cochet M (2007) Evaporation de gouttelettes polydispersées dans un écoulement de canal fortement turbulent. analyse de la formation du mélange diphasique par image de fluorescence. PhD thesis, INPT

Cochet M, Bazile R, Ferret B, Cazin S (2009) Evaporation of polydispersed droplets in a highly turbulent channel flow. Exp Fluids 47(3):379–394

Erdmann JC, Gellert RI (1976) Particle arrival statistics in laser anemometry of turbulent-flow. Appl Phys Lett 29(7):408–411

Harstad KG, Le Clercq PC, Bellan J (2003) Statistical model of multicomponent-fuel drop evaporation for many-drop flow simulations. Aiaa J 41(10):1858–1874

Hoesel W, Rodi W (1977) New biasing elimination method for laser-doppler velocimeter counter processing. Rev Sci Instrum 48(7):910–919. doi:10.1063/1.1135131

Hubbard G, Denny V, Mills A (1975) Droplet evaporation: Effects of transients and variable properties. Int J Heat Mass Transf 18(9): 1003–1008

Kapulla R, Najera SB (2006) Operation conditions of a phase doppler anemometer: droplet size measurements with laser beam power, photomultiplier voltage, signal gain and signal-to-noise ratio as parameters. Meas Sci Technol 17:221–227

Karpetis A, Gomez A (2000) An experimental study of well-defined turbulent nonpremixed spray flames. Combust Flame 121:1–23

Koch J, Hanson R (2003) Temperature and excitation wavelength dependencies of 3-pentanone absorption and fluorescence for plif applications. Appl Phys B 76:319–324

Marchisio DL, Fox RO (2005) Solution of population balance equations using the direct quadrature method of moments. J Aerosol Sci 36(1):43–73

McGraw R (1997) Description of aerosol dynamics by the quadrature method of moments. Aerosol Sci Technol 27:255–265

Modica V, Morin C, Guibert P (2007) 3-pentanone lif at elevated temperatures and pressures: measurements and modeling. Appl Phys B 87:193–204

Moreau F (2010) Évaporation et dispersion d'un spray bi-composant dans un écoulement de canal chauffé fortement turbulent: une approche expérimentale. PhD thesis, Institut National Polytechnique de Toulouse, Université de Toulouse

Orain M, Grisch F, Rossow B (2008) Application de l'imagerie de fluorescence induite par laser á la mesure de richesse locale dans un spray multicomposants. In: Congrès Francophone de Techniques Laser, CFTL 2008, Futuroscope, 16–19 Sept 2008

Sirignano W (1999) Fluid dynamics and transport of droplets and sprays. Cambridge University Press, Cambridge

Sornek RJ, Dobashi R, Hirano T (2000) Effect of turbulence on vaporization, mixing, and combustion of liquid-fuel sprays. Combust Flame 120(4):479–491

Spalding (1951) Combustion of fuel particles. Fuel 30:121–130

Videto BD, Santavicca DA (1991) A turbulent-flow system for studying turbulent combustion processes. Combust Sci Technol 76(1–3):159–164